Nanoscale Advances

ROYAL SOCIETY OF CHEMISTRY

PAPER

View Article Online
View Journal | View Issue

Cite this: *Nanoscale Adv.*, 2025, **7**, 329

Charge-switchable zwitterionic nanomagnets for wastewater remediation†

Sohel Reja * and Sukumaran Vasudevan

Enormous amounts of toxic synthetic dyes and inorganic contaminants, such as heavy metals, are regularly discharged into local water bodies unregulated and untreated through effluents from a wide range of industries. Designing industrial methodologies that limit or eliminate the unloading of harmful substances in the surrounding environment has become a requisite for sustainable growth. Although the magnetic separation-based adsorption technique seems quite promising, the functional moieties on the nanoparticle surface often restrict the choice of target pollutants, limiting their universal applicability. Here, we explore the utility of a zwitterion-coated magnetic adsorbent for the easy separation of both positively and negatively charged contaminants from water. Water-dispersible monodispersed nitrilotriacetic acid-functionalized superparamagnetic iron oxide nanoparticles (NTA@SPIONs) were prepared on a large scale following a simple one-pot route. The zwitterionic nanoparticles exhibit surface charge reversibility with a change in pH. The charge-switching property of the nanomaterial was exploited for the removal of cationic and anionic contaminants, such as dyes and heavy metal ions. By proper tuning of the medium pH, methylene blue (MB), a cationic dye, and Congo red (CR), a benzidine-based anionic azo dye, were separated from the aqueous dispersion with the help of the NTA@SPIONs. Under the same working principle, chromium, a highly toxic heavy metal both in cationic and anionic form, was successfully separated from the contaminated water. Low-gradient magnetic separation makes the process rapid, easy, and efficient, and also avoids the chances of secondary pollution.

Received 1st September 2024
Accepted 21st November 2024

DOI: 10.1039/d4na00730a

rsc.li/nanoscale-advances

Introduction

Wastewater remediation has remained an active research field and has become increasingly more relevant, given the dire need for a robust and efficient strategy for tackling water pollution.[1–5] The booming population and unplanned urbanisation coupled with poor management policies have paved the way for ecological imbalance by infusing a heavy influx of hazardous chemicals, such as dyes and heavy metals, into the biota. High toxicity and reduced light penetration, resulting in lowered photosynthesis, adversely affect aquatic life, and the hazardous chemicals also become a prominent issue once they enter the associated food chains.[6] The intricate aromatic backbone makes the dyes immune to light, heat and oxidation, and consequently, biodegradation. Acute exposure to cationic dyes such as methylene blue (MB) can cause elevated heart rate, vomiting, shock, Heinz body formation, cyanosis, jaundice, quadriplegia and tissue necrosis.[7] Biotransformation of benzidine-based anionic azo dyes such as Congo red (CR) can produce carcinogenic benzidine and amine groups. Prolonged exposure to CR can cause kidney and heart ailments and diseases such as amyloidosis, a case of abnormal protein accumulation within the extracellular space in tissues.[8]

The presence of toxic heavy metals, such as lead, mercury, arsenic, cobalt, nickel, cadmium and chromium, at elevated concentrations adversely impacts aquatic organisms by disrupting their natural metabolism. As a result, the circulation of bioaccumulated heavy metals among the organisms within a specific food chain ultimately results in biomagnification.[9] Chromium poisoning, a result of untreated wastewater rich in chromium from tannery effluents, ore processing industry, steel–cement industry and electroplating, remains a constant threat. Chromium, in its highest oxidation state (Cr(VI)), is a highly toxic carcinogen and causes oxidative stress. Although Cr(III) is less lethal than its fully oxidised counterpart, the rapid oxidation of Cr(III) to Cr(VI) in the natural environment ultimately leads to the same catastrophic end. Prolonged chromium exposure can damage several organs, such as the liver and kidneys, and can trigger a special kind of skin allergy, chrome ulcers. Acute chromium poisoning can cause vomiting, diarrhoea, haemorrhage and cardiovascular shock, a result of blood loss into the gastrointestinal tract.[7]

A wide range of methodologies for wastewater treatment have been developed, such as ultrafiltration, coagulation, membrane separation, oxidation, ozonolysis, chlorination, and

Department of Inorganic and Physical Chemistry, IISc Bangalore, India. E-mail: sohelreja@iisc.ac.in

† Electronic supplementary information (ESI) available. See DOI: https://doi.org/10.1039/d4na00730a

adsorption.[10–14] Among the various methodologies available, adsorption has remained the front-runner since it offers high efficiency, simple design and minimal energy and cost demand. Although carbon and carbon-based composite materials have been excellent candidates for adsorption, demanding separation and regeneration steps, as well as chances of secondary pollution, have remained a pressing issue. Equipped with impressive biocompatibility, scope of economic scaled-up production, ease of surface modification and high magnetisation, which can be exploited for magnetic separation and recovery, iron oxide nanoparticles have attracted considerable attention as promising adsorbent materials for water remediation. Surface functionalised magnetic nanoparticles with organic chelating moieties anchored to the particle surface have been excellent choices since they offer easy separation, good efficiency and reduced chances of secondary pollution.[15,16] Dispersing magnetic nanoparticles in contaminated water and their subsequent removal, along with the adsorbed contaminants, by a low magnetic field gradient is a simple yet appealing technique that is, in principle, more selective and efficient than centrifugation or filtration.[11,17–19] The utility of this procedure was first demonstrated in 2006 when arsenic in contaminated water was successfully adsorbed on superparamagnetic iron oxide nanoparticles (SPIONs) dispersed in the solution and subsequently removed using a hand-held magnet.[20,21] Apart from arsenic, numerous other contaminants arising from natural sources and modern manufacturing processes also pose a serious threat.[22] The most common pollutants in wastewater are metal ions, dyes, phenols, pesticides, and a wide spectrum of aromatic compounds.[4,12,23,24]

Although the magnetic separation-based adsorption technique seems quite promising, the functional moieties on the nanoparticle surface often restrict the choice of target pollutants, limiting their universal applicability.[25] The utility of the magnetic separation technique would be greatly enhanced if the functionalised nanoparticles could separate a broader range of contaminants present in water. Tailoring the nanoparticle surface with charge-switchable zwitterions may prove to be an efficient strategy for targeting a broader spectrum of charged pollutants, both cationic and anionic.

Here, we report the utility of water-dispersible nitrilotriacetic acid-functionalised superparamagnetic iron oxide nanoparticles (NTA@SPIONs), which are zwitterionic in nature and can, therefore, rapidly separate either anionic or cationic pollutants from water depending upon pH, by a simple hand-held bar magnet. The zwitterion-functionalization strategy holds the possibility of covering a broader spectrum of charged pollutants, including toxic dyes and heavy metals.

Experimental

Materials

Ferric nitrate nonahydrate ($Fe(NO_3)_3 \cdot 9H_2O$), isopropanol, acetone, ethanol, and toluene were purchased from SD Fine Chemicals. Oleic acid, trisodium nitrilotriacetate monohydrate ($Na_3NTA \cdot H_2O$), and 1-octadecene were provided by Sigma-Aldrich. All chemicals were used as received without further purification.

Preparation of NTA-coated iron oxide nanoparticles

NTA-functionalized monodispersed superparamagnetic iron oxide nanoparticles were prepared following a previously reported modified thermal decomposition route by our group.[26] In a typical synthesis of 13 nm NTA@SPIONs, 30 mmol of $Fe(NO_3)_3 \cdot 9H_2O$ was added to 300 mL isopropanol and 120 mL octadecene. After a 30 minute workup at 150 °C, 180 mmol of oleic acid was added, and the reaction mixture was heated to reflux at 320 °C for 2 hours under an argon blanket and continuous stirring. After the reaction was over, the solution was left to cool, followed by adding 90 mmol of $Na_3NTA \cdot H_2O$ in a 2 : 1 mixture of 450 mL ethanol/water and 120 mL toluene. The reaction mixture was heated for 4 hours at 80 °C. Finally, the NTA@SPIONs were separated magnetically and washed thoroughly with water, ethanol, and acetone.

Characterisation

The phase composition of the nanocrystals was determined using a PANalytical Empyrean X-ray diffractometer equipped with a Pixcel 3D detector with Cu-K_α radiation. The size and shape evolution of the nanocrystals were studied with a JEOL JEM 2100F transmission electron microscope. Magnetic properties were measured with a Quantum Designs PPMS 9T 639. A Bruker ALPHA-II Compact ATR-FTIR was used to perform infrared spectroscopy. A Malvern Zetasizer ZS was been used for zeta potential analysis.

Batch adsorption study

Batch adsorption studies were conducted by adding NTA@SPIONs to the contaminant solution, followed by sonicating in a bath sonicator for a certain period. After completion, the adsorbent was separated from the dispersion with a bar magnet. The supernatant solution was then analysed to determine the remaining pollutant concentration. For the single-factor batch adsorption studies, the target parameter was systematically varied while keeping the other parameters constant. A set of solutions with different initial concentrations were tested for the adsorption isotherm study. For the adsorption kinetics study, the adsorption time was varied from 2 minutes to 120 minutes. MB and CR standard solutions were made by dissolving appropriate amounts of the dyes in milli-Q water. $Cr_2O_7^{2-}$ and Cr^{3+} standard solutions were made by dissolving potassium dichromate and chromium chloride in Milli-Q water, respectively. The remaining pollutant concentration in the supernatant (after the magnetic separation) was estimated spectroscopically. Following Lambert–Beer's law, first, the calibration plots were obtained by measuring the UV-vis spectra of known concentrations of the pollutants. The molar absorption coefficient obtained from the slope of the absorbance *vs.* concentration plot was used further to determine the concentration of the unknown solution. MB and CR were estimated spectroscopically at the wavelengths of 664 nm and 498 nm, respectively.[27,28] Both $Cr_2O_7^{2-}$ and Cr^{3+} were estimated using the 1,5-diphenylcarbazide (DPC) method.[29–32] Removal efficiency (%) and the adsorption capacity, q_e, (mg L^{-1}), were calculated following the mathematical relationships given by

$$\text{Removal efficiency}(\%) = \frac{c_0 - c_e}{c_0} \times 100\%$$

$$q_e = \frac{c_0 - c_e}{m} \times V$$

where c_0 is the initial and c_e is the equilibrium dye concentration after adsorption, m is the adsorbent dosage, and V is the volume of the dye solution.

Results and discussion

Synthesis of NTA-coated iron oxide nanoparticles

The water-dispersible NTA@SPIONs were prepared on a large scale by a recently reported one-pot thermal decomposition route with minor modifications (Scheme 1).[26] The synthesis involves the alcoholic hydrolysis of a simple iron salt into iron hydroxide, which forms the precursor oleate complex following the addition of oleic acid. The *in situ* formed iron oleate complex was then thermally decomposed to produce highly monodispersed SPIONs. Subsequent addition of $Na_3NTA{\cdot}H_2O$ solution can efficiently transfer the oleate-coated SPIONs from the non-polar solvent to the aqueous phase without the need for separation from the crude reaction mixture. The water-dispersible NTA@SPIONs were then separated from the reaction medium by a hand-held bar magnet. The modified thermal decomposition route offers the twin benefits of simplicity and scalability (ESI, Fig. S1†).

The phase composition of the NTA@SPIONs was characterised by powder X-ray diffraction (PXRD) (Fig. 1a). Iron oxide nanoparticles prepared *via* the thermal decomposition route have often been reported to exhibit a mixed-phase composition-ferrimagnetic magnetite and antiferromagnetic wustite.[33] Rietveld refinement of the PXRD patterns of the NTA@SPIONs indicated a phase composition corresponding to 99.3% magnetite (Fe_3O_4; ref. no. 96-900-5840) and 0.7% wustite (FeO; ref. no. 96-900-9768). The reflection peaks can be assigned to the (220), (311), (400), (422), (511) and (440) planes of the cubic magnetite phase. The crystallite size, 11 nm, estimated using the Debye–Scherrer equation, is in good agreement with the TEM results (13 nm) shown in Fig. 1b.

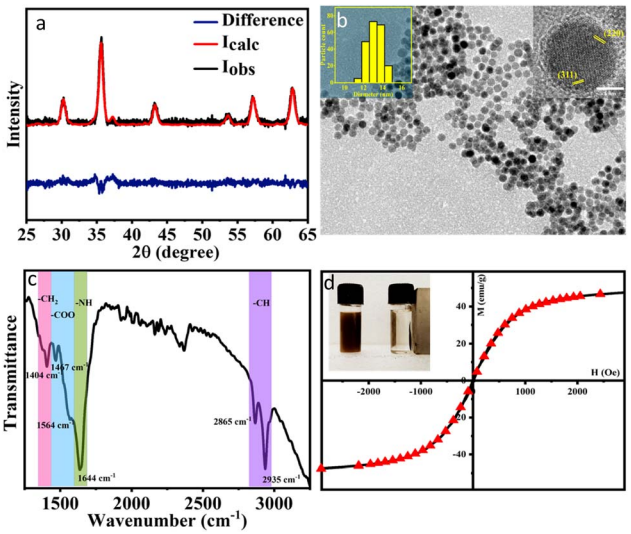

Fig. 1 (a) PXRD pattern of the NTA@SPIONs. The red line is the best fit from a Rietveld analysis. The difference between the experiment and the Rietveld fit is shown in blue. (b) TEM image of the NTA@SPIONs. The inset on the right shows the HRTEM; indexing is based on the spinel phase of iron oxide. The inset on the left shows the particle size distribution. (c) The ATR-IR spectrum with bands assigned. (d) The isothermal (300 K) *M–H* plot and the Langevin equation fit. The inset shows a photograph of NTA@SPIONs separation from an aqueous dispersion with a bar magnet.

A TEM image of the NTA@SPIONs shows a fairly monodisperse distribution, confirming the retainment of the superior particle attributes of the thermal decomposition route[34] (Fig. 1b). The lattice fringes in the HRTEM (inset of Fig. 1b) matched well with the (311) and (220) planes of the spinel phase magnetite (the indexed SAED and FFT patterns are provided in the ESI, Fig. S1†). The particle size distribution histogram showed an average particle diameter of 13 nm (inset of Fig. 1b). A certain degree of aggregation was observed in the TEM image; this may be a consequence of inter-particle hydrogen bonding between the surface-attached NTA groups.

The ATR-IR spectrum (Fig. 1c) of the NTA@SPIONs confirmed the presence of NTA moieties on the particle surface. The spectrum exhibited characteristic peaks for the N–H bending vibrational mode (1644 cm^{-1}), as well as the asymmetric and symmetric modes of the carboxylic group that appear at 1564 and 1467 cm^{-1}, respectively. The bands observed at 2935 and 2865 cm^{-1} are probably due to stretching modes of the methylene groups arising from trace amounts of undetached oleic acid.

The isothermal *M–H* measurements of the NTA@SPIONs recorded at room temperature (300 K) are shown in Fig. 1d. The observed zero coercivity of the *M–H* curve signifies the single-domain nature of the nanoparticles, indicating their superparamagnetic behaviour. This was confirmed by fitting the experimental *M–H* curve with a modified Langevin function-

$$M = M_0 L(x) + \chi H$$

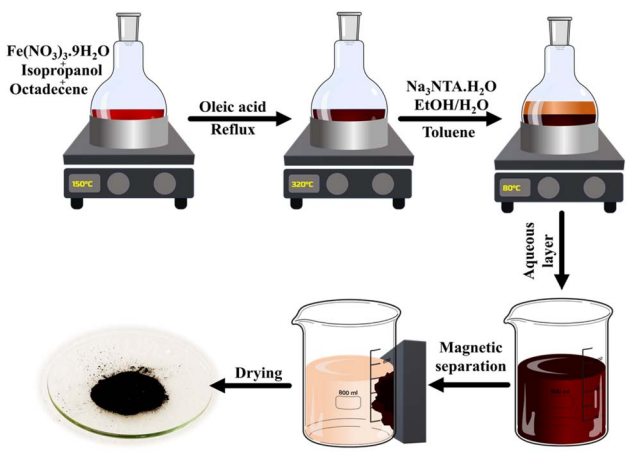

Scheme 1 Graphical representation of NTA@SPIONs synthesis.

where $L(x) = [\coth(x) - (1/x)]$ is the Langevin function, M_0 the saturation magnetisation, and $x = \mu_p H/k_B T$, where μ_p is the particle magnetic moment, k_B the Boltzmann constant, and x is the susceptibility of the ferrimagnetic nanoparticles, as predicted by Néel for particles with antiferromagnetic interactions. The saturation magnetisation (M_0) estimated from the Langevin fitting parameters, 53 emu g^{-1} of NTA@SPIONs, is comparable to that reported for SPIONs of similar dimensions.[33] A consequence of the large magnetisation values of the NTA@SPIONs is that they are easily and rapidly separable from aqueous dispersions by low magnetic fields, such as a hand-held bar magnet (inset of Fig. 1d).

The NTA@SPIONs are readily dispersible in water. The dispersions are stable, and DLS measurements indicate little or no aggregation even after extended periods (ESI, Fig. S2†). A remarkable feature of the aqueous dispersions of NTA@SPIONs is the pH dependence of the zeta potential (Fig. 2a). In the pH range of 3 to 7, the zeta potential of the NTA@SPIONs dispersions changes its value from positive (+31 eV at pH = 3) to negative (−28 eV at pH = 7) with the isoelectric point occurring at pH 5.10 (Fig. 2b). It is clear from the magnitude of the zeta potential values that the dispersions are stabilised by electrostatic repulsion. The surface charge reversal exhibited by the NTA@SPIONs with pH may be attributed to the zwitterionic nature of the NTA groups attached to the particle surface. NTA is a readily available amino-polycarboxylic acid which finds extensive use as a chelating agent in the detergent industry.[35,36] The pK_a values of NTA at 25 °C are 1.8, 2.6, and 9.8.[37] In the pH range between these two extremes, the species remains as a doubly charged carboxylate anion (a result of the dissociation of the first two carboxyl groups); the unusually high third dissociation constant may be understood by considering a zwitterionic form of NTA, where the third pK_a corresponds to the deprotonation of the protonated amine group and not the carboxyl group.[38–41] The NTA groups are probably coordinated to the surface, either as a monodentate or bidentate ligand, similar to how citric acid coordinates to the surface of iron oxide nanoparticles.[42–44] From the infrared spectrum (Fig. 1c), it is difficult to establish the exact nature of the coordination, but the fact that at pH > 5.1, the zeta potential is negative readily implies that at least one of the three carboxylic groups of the NTA is free and can undergo deprotonation. At the isoelectric point, the species exists as a zwitterion with the carboxylic group deprotonated and the proton attached to the amino centre. At pH < 5.1, both the carboxylic and amino groups are protonated, imparting a net positive charge to the NTA@SPIONs. A cartoon representation of the protonation and deprotonation events at various pH values is shown in Fig. 2c. In the cartoon, it is assumed that the NTA is coordinated as a bidentate ligand on the surface of the SPIONs. This is not an unreasonable assumption as the magnitudes of the zeta-potential values, irrespective of the sign, in the two pH ranges are comparable, suggesting that a single proton is involved in both events.

Charge reversal with pH can be exploited for the selective adsorption of target molecules that have a charge opposite to that of the NTA@SPIONs. The NTA@SPIONs, along with the adsorbed contaminant, can then be removed from the dispersion with a simple hand-held bar magnet. The collected magnetic adsorbent material may then be treated in a suitable eluting medium for further reuse.

The versatility of the NTA@SPIONs for water remediation is demonstrated in Fig. 3, where it is shown that chromium, both as the cation (Cr^{3+}) and anion ($Cr_2O_7^{2-}$), can be adsorbed on

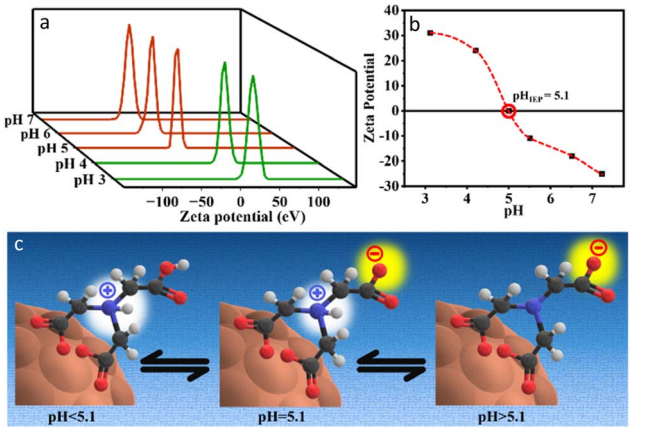

Fig. 2 (a) Zeta potential distribution of NTA@SPIONs dispersions at different pH values, (b) determination of isoelectric point, and (c) a cartoon showing the possible protonation/deprotonation events at different pH values.

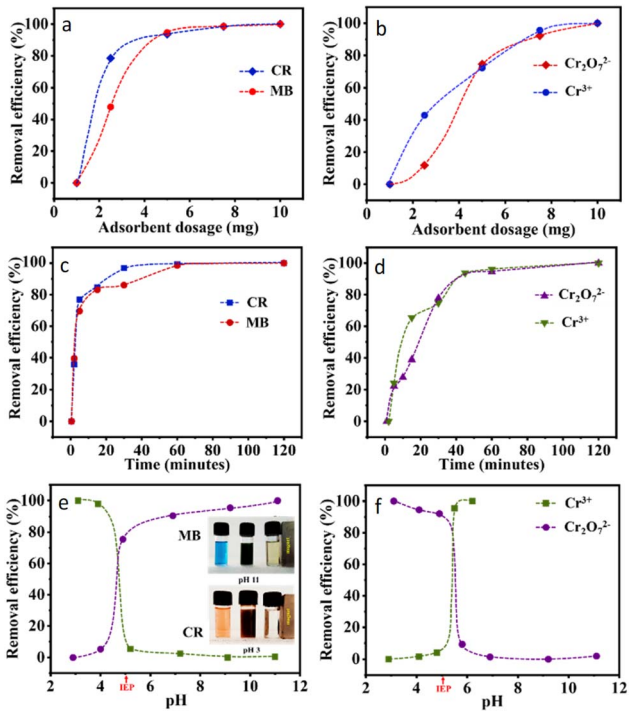

Fig. 3 The normalised removal efficiency of the cationic dye, MB, and the anionic dye, CR, with different (a) adsorbent dosage, (c) time and (e) pH. The normalised removal efficiency of Cr^{3+} and $Cr_2O_7^{2-}$ with (b) adsorbent dosage, (d) time and (f) pH. The inset of (e) shows photographs of dye removal by NTA@SPIONs, followed by magnetic separation.

NTA@SPIONs dispersed in the solution and removed from the dispersion by a hand-held magnet. The adsorption of Cr^{3+} occurs at pH > 5.1 when the NTA@SPIONs are negatively charged and at pH < 5.1 for $Cr_2O_7^{2-}$ when the adsorbent is positively charged (Fig. 3f). Uptake measurements indicate a maximum uptake of 2.56×10^{-4} mol g^{-1} for Cr^{3+} at pH 5.5 and 7.89×10^{-5} mol g^{-1} for $Cr_2O_7^{2-}$ at pH 3. For both Cr^{3+} and $Cr_2O_7^{2-}$ the adsorption follows the Langmuir isotherm (ESI, Fig. S3†). The value of the separation factor (RL) lies in the range of 0 to 1, confirming favourable adsorption. To estimate maximum adsorption capacity, the removal efficiency was studied as a function of adsorbate concentration. At lower heavy metal concentrations, the removal efficiency was relatively higher since the relative number of adsorption sites outweighed the number of adsorbate molecules (ESI, Fig. S3†). The time-dependence of the uptake follows pseudo-second-order kinetics, characteristic of chemisorption, with rate constants of 0.054 g mg^{-1} min^{-1} and 0.046 g mg^{-1} min^{-1}, respectively (ESI, Fig. S4†). The time dependency of removal efficiency shows that the adsorption process is almost complete within 45 minutes of reaction time. In the beginning, the adsorption process is rapid since a larger number of free sites are available on the adsorbent surface; however, as time passes, a reduced concentration of free sites makes the adsorption process slow (Fig. 3d). It should be noted that at low adsorbate concentrations, the adsorption process is inevitably faster; however, to properly ascertain the adsorption kinetics, a higher adsorbate concentration was chosen. To estimate the optimum quantity of NTA@SPIONs required for the adsorption process, the removal efficiency was studied as a function of adsorbent dosage. The heavy metal concentration being constant, the lower adsorbent dosage resulted in a lower removal efficiency since the number of adsorbates outweighed the number of adsorbent sites. With increasing adsorbent dosage, a saturation state was reached where any further increase in adsorption sites did not increase the efficiency (Fig. 3b). The loaded NTA@SPIONs can be completely removed from the dispersion by magnetic separation. Following the adsorption of $Cr_2O_7^{2-}$ and subsequent magnetic separation, the NTA@SPIONs were further characterised with PXRD and TEM to investigate possible post-adsorption compositional and dimensional changes of the nanoparticles. The PXRD plot indicates the retainment of the original phase after pollutant adsorption (ESI, Fig. S5†). The TEM image suggests there is no change in the dimensions or morphology of the NTA@SPIONs after pollutant adsorption (ESI, Fig. S6†). Energy dispersive spectroscopy (EDS) of the $Cr_2O_7^{2-}$-loaded NTA@SPIONs confirmed the adsorption of chromium on the nanoparticle surface (ESI, Fig. S7†). Chromium, a known carcinogen, is toxic in drinking water, and its removal by magnetic separation using NTA@SPIONs shows promise for point-of-use water remediation.

The use of the NTA@SPIONs for wastewater remediation is not limited to the removal of toxic heavy metals but can also be used for the removal of toxic synthetic dyes that exist either in the cationic or the anionic form. Here, we consider the removal of the cationic dye, MB, and the anionic dye, CR, from their aqueous solutions. As expected, for the cationic dye MB, the removal efficiency decreased with a decrease in pH, while for the anionic dye CR, the trend is just the opposite (Fig. 3e). The adsorption for both dyes follows the Langmuir isotherm (ESI, Fig. S3†) with a maximum uptake of 1.4×10^{-4} mol g^{-1} and 3.93×10^{-4} mol g^{-1} for MB and CR, respectively. The adsorption process follows pseudo-second-order kinetics with rate constants of 0.202 g mg^{-1} min^{-1} for MB and 0.052 g mg^{-1} min^{-1} for CR (ESI, Fig. S4†). The order of the kinetics indicates a strong chemical interaction between the dye molecules and the NTA@SPIONs. The time and adsorbent dosage dependency of removal efficiency follows the same trend as that of chromium (Fig. 3a and c). The attainment of the equilibrium adsorption capacity within 30–45 minutes indicates rapid adsorption by the NTA@SPIONs. As shown in the inset photographs of Fig. 3e, the dye-adsorbed NTA@SPIONs can be completely removed from the dispersion with a small bar magnet.

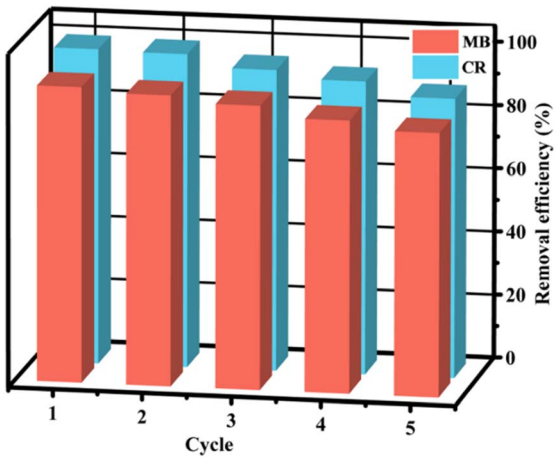

Fig. 4 Removal efficiency of MB and CR as a function of the number of cycles.

An essential requirement for a material to be an ideal adsorbent for water remediation is its reusability without any significant loss in removal efficiency. For the removal of the cationic and anionic dyes from water, the NTA@SPIONs exhibited a minimal loss in removal efficiency even after five

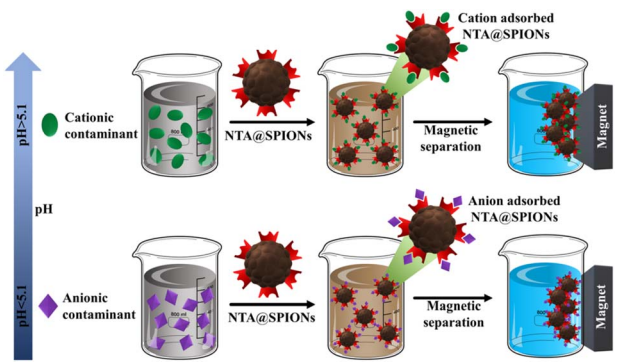

Scheme 2 Graphical representation of the pollutant separation process by NTA@SPIONs.

cycles (Fig. 4). Additionally, simple magnetic separation facilitates efficient lossless recovery of the adsorbent material. However, the adsorbent recyclability study for the cationic and anionic chromium species was challenging since a suitable eluting medium necessary for desorption was not identifiable. Although simple acid/base solutions have been known as an eluting medium, estimating efficiencies is an issue.

Conclusions

In summary, we have demonstrated that NTA@SPIONs exhibit surface charge reversibility, changing from positive to negative when pH changes from acid to base. The NTA@SPIONs were synthesised by a simple, scalable, one-pot preparative scheme that gave monodisperse superparamagnetic nanoparticles, which could be separated from the medium under low magnetic field gradients. Zeta potential measurements indicate that the stability of the NTA@SPIONs aqueous dispersions is due to electrostatic repulsion between the particles. A remarkable property of the NTA@SPIONs is that the sign of the zeta potential changes from positive to negative when the pH changes from 3 to 7 with the isoelectric point at pH 5.1. This property is a consequence of the zwitterionic property of the capping NTA moieties. Charge reversal with pH can be exploited to selectively adsorb target molecules that have a charge opposite to that of the NTA@SPIONs. The NTA@SPIONs, along with the adsorbed contaminant, can then be removed from the dispersion with a simple hand-held bar magnet, resulting in clean, decontaminated water (Scheme 2). The NTA@SPIONs phase composition, dimensions and morphology remain intact after pollutant adsorption, and there is no evidence of adsorbent-leaching. Irrespective of the adsorbate species, the adsorption process was completed in 30–45 minutes, demonstrating rapid separation. Toxic synthetic dyes and heavy metal ions are prominent water pollutants. Two well-known representatives, positively and negatively charged, from each of the above-mentioned classes of pollutants were subjected to adsorptive removal by NTA@SPIONs. Assuming the interaction to be electrostatic in nature between the adsorbate and the absorbent, it may be possible to separate a diverse range of charged pollutants under the same working principle.

Data availability

The authors confirm that the relevant data backing the findings of the present study are available in the main article and the corresponding ESI.† Raw data supporting the study are available from the corresponding author upon reasonable request.

Conflicts of interest

The authors declare there are no conflicts of interest.

Acknowledgements

The authors acknowledge support from the Chemical Science Division facility, IISc, for TEM, PXRD, and IR analysis.

Notes and references

1 S. Das, N. Mitra, J. Wan, A. Khan, T. Chakraborty and M. B. Ray, *Micropollutants in Wastewater: Fate and Removal Processes*, 2016, DOI: 10.5772/65644.
2 S. R. Dhokpande, S. M. Deshmukh, A. Khandekar and A. Sankhe, *Sep. Purif. Technol.*, 2024, **350**, 127868.
3 N. S. Topare and V. S. Wadgaonkar, *Mater. Today: Proc.*, 2023, 77, 8–18.
4 S. Dutta, B. Gupta, S. K. Srivastava and A. K. Gupta, *Mater. Adv.*, 2021, **2**, 4497–4531.
5 S. Ye, Y. Chen, X. Yao and J. Zhang, *Chemosphere*, 2021, **273**, 128503.
6 M. Perwez, H. Fatima, M. Arshad, V. K. Meena and B. Ahmad, *Int. J. Environ. Sci. Technol.*, 2023, **20**, 5697–5714.
7 F. T. Geldasa, M. A. Kebede, M. W. Shura and F. G. Hone, *RSC Adv.*, 2023, **13**, 18404–18442.
8 J. K. Sahoo, S. K. Paikra, M. Mishra and H. Sahoo, *J. Mol. Liq.*, 2019, **282**, 428–440.
9 A. E. Gahrouei, A. Rezapour, M. Pirooz and S. Pourebrahimi, *Desalin. Water Treat.*, 2024, **319**, 100446.
10 B. Natarajan, P. Kannan, J. A. Rather and R. A. Sheikh, *J. Taiwan Inst. Chem. Eng.*, 2023, **147**, 104942.
11 A. Lourens, A. Falch and R. Malgas-Enus, *J. Mater. Sci.*, 2023, **58**, 2951–2970.
12 H. K. Okoro, S. Pandey, C. O. Ogunkunle, C. J. Ngila, C. Zvinowanda, I. Jimoh, I. A. Lawal, M. M. Orosun and A. G. Adeniyi, *Emerging Contam.*, 2022, **8**, 46–58.
13 K. Q. Jabbar, A. A. Barzinjy and S. M. Hamad, *Environ. Nanotechnol., Monit. Manage.*, 2022, **17**, 100661.
14 Z. Iqbal, M. S. Tanweer and M. Alam, *J. Water Process Eng.*, 2022, **46**, 102641.
15 L. Mohammed, H. G. Gomaa, D. Ragab and J. Zhu, *Particuology*, 2017, **30**, 1–14.
16 K. K. Kefeni, B. B. Mamba and T. A. M. Msagati, *Sep. Purif. Technol.*, 2017, **188**, 399–422.
17 C. Liosis, A. Papadopoulou, E. Karvelas, T. E. Karakasidis and I. E. Sarris, *Materials*, 2021, **14**, 7500.
18 V. Sharma, H. Singh, S. Guleria, N. Bhardwaj, S. Puri, S. K. Arya and M. Khatri, *Environ. Nanotechnol., Monit. Manage.*, 2022, **18**, 100716.
19 X. Qu, J. Brame, Q. Li and P. J. J. Alvarez, *Acc. Chem. Res.*, 2013, **46**, 834–843.
20 C. T. Yavuz, J. T. Mayo, W. W. Yu, A. Prakash, J. C. Falkner, S. Yean, L. Cong, H. J. Shipley, A. Kan, M. Tomson, D. Natelson and V. L. Colvin, *Science*, 2006, 964–967.
21 S. Scurti, S. Dattilo, D. Gintsburg, L. Vigliotti, A. Winkler, S. C. Carroccio and D. Caretti, *ACS Omega*, 2022, **7**, 10775–10788.
22 A. Saravanan, P. S. Kumar, S. Jeevanantham, S. Karishma, B. Tajsabreen, P. R. Yaashikaa and B. Reshma, *Chemosphere*, 2021, **280**, 130595.
23 K. H. H. Aziz, F. S. Mustafa, K. M. Omer, S. Hama, R. F. Hamarawf and K. O. Rahman, *RSC Adv.*, 2023, **13**, 17595–17610.

24 A. V. Samrot, C. S. Sahithya, A. J. Selvarani, S. Pachiyappan and S. U. S. Kumar, *Int. J. Nanomed.*, 2019, **14**, 8105–8119.
25 K. Gupta, P. Joshi, R. Gusain and O. P. Khatri, *Coord. Chem. Rev.*, 2021, **445**, 214100.
26 S. Reja, M. Kumar and S. Vasudevan, *Nanoscale Adv.*, 2024, 3857–3864.
27 X. Zhang, P. Zhang, Z. Wu, L. Zhang, G. Zeng and C. Zhou, *Colloids Surf., A*, 2013, **435**, 85–90.
28 S. Yesmin, M. Mahiuddin, A. B. M. N. Islam, K. M. R. Karim, P. Saha, M. A. R. Khan and H. M. Ahsan, *ACS Omega*, 2024, **9**, 10727–10737.
29 A. Wiryawan, R. Retnowati and R. Y. P. Burhan, *J. Environ. Eng. Sustain. Tech.*, 2018, **5**, 37–46.
30 A. Lace, D. Ryan, M. Bowkett and J. Cleary, *Int. J. Environ. Res. Public Health*, 2019, **16**, 1803.
31 T. Shigematsu, S. Gohda, H. Yamazaki and Y. Nishikawa, *Bull. Inst. Chem. Res., Kyoto Univ.*, 2007, **55**, 429–440.
32 A. Wiryawan, R. Retnowati, P. Burhan and S. Syekhfani, *Journal of Environmental Engineering and Sustainable Technology*, 2018, **5**, 37.
33 R. Chalasani and S. Vasudevan, *J. Phys. Chem. C*, 2011, **115**, 18088–18093.
34 J. Park, K. An, Y. Hwang, J. E. G. Park, H. J. Noh, J. Y. Kim, J. H. Park, N. M. Hwang and T. Hyeon, *Nat. Mater.*, 2004, **3**, 891–895.
35 T. Egli, M. Bally and T. Uetz, *Biodegradation*, 1990, **1**, 121–132.
36 J. K. Jang, I. S. Chang, H. Moon, K. H. Kang and B. H. Kim, *Biotechnol. Bioeng.*, 2006, **95**, 772–774.
37 K. A. Krishnan, *Colloids Surf., A*, 2008, **317**, 344–351.
38 J. D. Oliver, B. L. Barnett and L. C. Strickland, *Acta Crystallogr., Sect. B:Struct. Sci.*, 1984, **40**, 377–381.
39 Y. Tomita and K. Ueno, *Bull. Chem. Soc. Jpn.*, 1963, **36**, 1069–1073.
40 E. R. Souaya, W. G. Hanna, E. H. Ismail and N. E. Milad, *Molecules*, 2000, **5**, 1121–1129.
41 X. Zhang, G. Pan, L. Hu, H. Wang and C. Wang, *Colloids Surf., A*, 2020, **605**, 125392.
42 Y. Sahoo, A. Goodarzi, M. T. Swihart, T. Y. Ohulchanskyy, N. Kaur, E. P. Furlani and P. N. Prasad, *J. Phys. Chem. B*, 2005, **109**, 3879–3885.
43 M. A. Dheyab, A. A. Aziz, M. S. Jameel, O. A. Noqta, P. M. Khaniabadi and B. Mehrdel, *Sci. Rep.*, 2020, **10**, 1–8.
44 N. Kallay and E. Matijević, *Langmuir*, 1985, **1**, 195–201.